

CoMI-IRL: Contrastive Multi-Intention Inverse Reinforcement Learning

Antonio Mone, Frans A. Oliehoek, Luciano Cavalcante Siebert

Delft University of Technology, the Netherlands

{a.mone, f.a.oliehoek, l.cavalcantesiebert}@tudelft.nl

Abstract

Inverse Reinforcement Learning (IRL) seeks to infer reward functions from expert demonstrations. When demonstrations originate from multiple experts with different intentions, the problem is known as Multi-Intention IRL (MI-IRL). Recent deep generative MI-IRL approaches couple behavior clustering and reward learning, but typically require prior knowledge of the number of true behavioral modes K^* . This reliance on expert knowledge limits their adaptability to new behaviors, and only enables analysis related to the learned rewards, and not across the behavior modes used to train them. We propose Contrastive Multi-Intention IRL (CoMI-IRL), a transformer-based unsupervised framework that decouples behavior representation and clustering from downstream reward learning. Our experiments show that CoMI-IRL outperforms existing approaches without a priori knowledge of K^* or labels, while allowing for visual interpretation of behavior relationships and adaptation to unseen behavior without full retraining.

1 Introduction

Inverse Reinforcement Learning (IRL) deals with tasks where the reward function is unknown or difficult to define by recovering a reward function from demonstrations [Ng and Russell, 2000]. IRL has progressed from modeling rewards as linear combination of features [Ng and Russell, 2000; Abbeel and Ng, 2004], through ambiguity reduction methods [Ziebart *et al.*, 2008; Ramachandran and Amir, 2007], to deep learning-based methods in generative adversarial [Ho and Ermon, 2016; Fu *et al.*, 2017] settings. However, these approaches assume all demonstrations share a unique goal. This is often not the case, as datasets can contain non-optimal and conflicting modes of behavior collected from multiple sources. Such problem is known as Multi-Intention IRL (MI-IRL) [Babes *et al.*, 2011].

MI-IRL addresses reward modeling in three ways: (i) as a linear combination of features in Expectation-Maximization (EM) [Babes *et al.*, 2011; Bighashdel *et al.*, 2023], (ii) through Bayesian methods [Choi and Kim, 2012; Michini

and How, 2012], and (iii) as neural networks in generative frameworks [Li *et al.*, 2017; Fu *et al.*, 2023; Hausman *et al.*, 2017], with the latter achieving most promising results. Deep learning-based methods typically couple behavior clustering and reward learning by introducing a latent code c , often sampled from a categorical distribution with K fixed categories. Each category represents a behavioral mode, a distinct pattern corresponding to an agent’s intention, which can be modeled by a reward function. Conceptually, these methods ask “How likely is a given trajectory to be generated by following a reward function associated with latent code c ?”.

Coupling behavior clustering and reward learning introduces key limitations. First, fixing K assumes knowledge of the true number of behavioral modes K^* , often unavailable and hard to specify, akin to the challenge of selecting cluster numbers in data analysis [Wang, 2010; Tibshirani *et al.*, 2001], risking misspecification. In settings where new behaviors are added, models with fixed K require full retraining. Methods inferring K from data have been explored (e.g., nonparametric Bayesian IRL [Choi and Kim, 2012]), however their application in continuous spaces is challenging due to computational limitations. Second, in coupled approaches the failure in one task can cascade and complicate diagnosis (i.e. it’s hard to verify if the model failed to learn the reward or to cluster behavior correctly). Finally, this coupled design hinders interpretability, since coupled methods allow to analyze behaviors only by deploying the latent-conditioned policies and not through the original dynamics.

In this paper, we address the limitations of coupled methods by investigating MI-IRL from a decoupled perspective, separating “what happened” (behavior clustering), from “why it happened” (reward learning). We propose Contrastive Multi-Intention IRL (CoMI-IRL), a transformer-based unsupervised framework that learns trajectory embeddings via contrastive training¹. The learned representations are grouped for their intrinsic patterns and not by reward likelihood. By inducing a similarity structure in the embedding space, we can discover clusters of behavioral modes via graph-based connectivity without knowing K . This reduces MI-IRL to independent single-intention IRL per cluster, also enabling direct adaptation to new behaviors.

¹The repository will be made available on GitHub after publication or upon request.

In our experiments, we analyze how the relationship between the assumed (K) and true (K^*) number of behavioral modes (i.e., $K \neq K^*, K = K^*$) impacts clustering and reward learning. We show how our approach avoids this problem, facilitates the interpretation of similarities in the dataset and can adapt to new behaviors without full retraining. Our results demonstrate that our design outperforms other approaches in both clustering quality and reward learning without requiring K , alleviating the limitations of coupled methods, enhancing MI-IRL adaptability to new behaviors.

2 Background

In this section, we formulate the MI-IRL problem and review the key concepts in contrastive learning applied in our work.

2.1 Multi-intention IRL

In multi-intention IRL, a finite-state Markov Decision Process without Rewards (MDP\mathcal{R}) is the tuple $(S, A, T, \gamma, b_0, \tau_1, \dots, \tau_D)$, where S is the state space, A is the action space, $T : S \times A \times S \rightarrow [0, 1]$ is the transition probability function, $\gamma \in [0, 1]$ is the discount factor, b_0 is the probability of starting in state s , and $\tau_i = (s_0, a_0, s_1, a_1, \dots, s_T, a_T)$ is the i^{th} trajectory in a dataset of D trajectories. Each trajectory is generated from the optimal policy of one of K^* behavioral modes, each corresponding to an intention mathematically represented by a reward function. Trajectories are assumed to be without labels, and the goal is to infer the number of behavioral modes and each respective reward function.

2.2 Contrastive Learning

Contrastive Learning (CL) is a self-supervised technique for learning representations by mapping similar (positive) examples closer in an embedding space, and dissimilar (negative) objects apart. CL is often applied to unsupervised sequence embedding methods with pretrained transformers to capture global semantics without requiring labels.

For example, BERT [Devlin *et al.*, 2019] prepends a special token called *CLS* to the beginning of every sequence. As the model processes the sequence, this token learns to collect information from all other elements, ending up as a single vector that summarizes the entire input [Qin *et al.*, 2023; Wang *et al.*, 2024; Zou *et al.*, 2024]. We use this concept to represent trajectories and distinguish behaviors: we treat each τ_i as a “sentence” and use the *CLS* token as a compact summary of the behavior.

Contrastive learning methods benefit from data augmentation [Deng *et al.*, 2023], but strong augmentations could disrupt behavior coherence. To form positive pairs without disrupting the coherence of the behavior, weak augmentations can be used. An effective strategy to form positive pairs is to create two dropout-augmented views of the input by passing each input sequence through the model twice, while all other trajectories in the batch serve as negative elements, following the intuition from [Gao *et al.*, 2021]. These dropout-augmented views can then be passed into a contrastive loss such as the symmetric InfoNCE [Oord *et al.*, 2018; Chen *et al.*, 2020], a central component of our approach that encourages informative and distinguishable embeddings. Since

InfoNCE is asymmetric with respect to the anchor, the symmetric version treats each view as an anchor in turn, ensuring both views contribute equally to the contrastive signal. The loss for a single view $z_{\tau_i}^1$ is

$$\ell(z_{\tau_i}^1, z_{\tau_i}^2) = -\log \frac{\exp(\text{sim}(z_{\tau_i}^1, z_{\tau_i}^2)/\rho)}{\sum_{k=1, k \neq i}^{2N} \exp(\text{sim}(z_{\tau_i}^1, z_{\tau_k}^2)/\rho)}, \quad (1)$$

and symmetric for $z_{\tau_i}^2$, where sim is cosine similarity, ρ is temperature and N is the number of trajectories in the batch.

In addition, we want to further distinguish embeddings so that learned representations can be consistently clustered. For this, regularization terms such as a Deep Info-Max (DIM) [Hjelm *et al.*, 2019] can help, by maximizing mutual information via Jensen-Shannon divergence (JSD) so that each local element of the input informs the whole representation. DIM trains a discriminator f_ϕ to give positive scores to pairs $f_\phi(z_{\tau_i}(\theta), z_{\tau_i(q)}(\theta))$ with the global summary paired with its own local features (joint pairs), and negative scores to pairs $f_\phi(z_{\tau_i}(\theta), z_{\tau_j(q)}(\theta))$ where $i \neq j$, so that:

$$\mathcal{L}_{\text{DIM}} = -\mathbb{E}_{P_J} [\log \sigma(f_\phi(z_{\tau_i}, z_{\tau_i(q)}))] - \mathbb{E}_{P_M} [\log(1 - \sigma(f_\phi(z_{\tau_i}, z_{\tau_j(q)})))] \quad (2)$$

where $\sigma(x) = \frac{1}{(1+e^{-x})}$ is the sigmoid function.

3 Contrastive Multi-Intention IRL

In this section we introduce CoMI-IRL, a framework that decouples behavior clustering and reward learning. Using a fully unsupervised contrastive approach, CoMI-IRL maps *quantile normalized* demonstrations into an embedding space via a *Behavioral Encoder (BE)* with *L2-normalized* outputs, followed by *Clustering*, defining single-intention groups for downstream *Reward Learning* (Figure 1). At its core, the BE, a Transformer Encoder [Vaswani *et al.*, 2017] with a pre-processing block, generates trajectory representations as *CLS* tokens to represent complex behaviors based on their intrinsic patterns (Section 3.1). As similar trajectories are grouped together, cluster labels are obtained via a graph-based method for the subsequent IRL step (Section 3.2). CoMI-IRL can be adapted to new behavior without full retraining (Section 3.3).

3.1 Behavioral Encoder Architecture

The first step is to embed trajectories in a latent space such that similar behaviors are grouped together. We base our approach on the Transformer model [Vaswani *et al.*, 2017] as it allows to create representations encoding information between distant timesteps through its attention mechanism. We quantile normalize the input trajectories [Bolstad *et al.*, 2003], independently mapping each dimension to a normal distribution, since the state-action spaces contain high-frequency elements with substantially different magnitudes.

Further, as states S_{τ_i} and actions A_{τ_i} of each input trajectory i -th have different dynamics, we encode them with two different pre-processing heads, one for each sequence [Chen *et al.*, 2021]. Each head applies a Random Fourier Features (RFF) encoding with Gaussian mapping [Tancik *et al.*, 2020; Zheng *et al.*, 2022; Li *et al.*, 2021], followed by a shallow

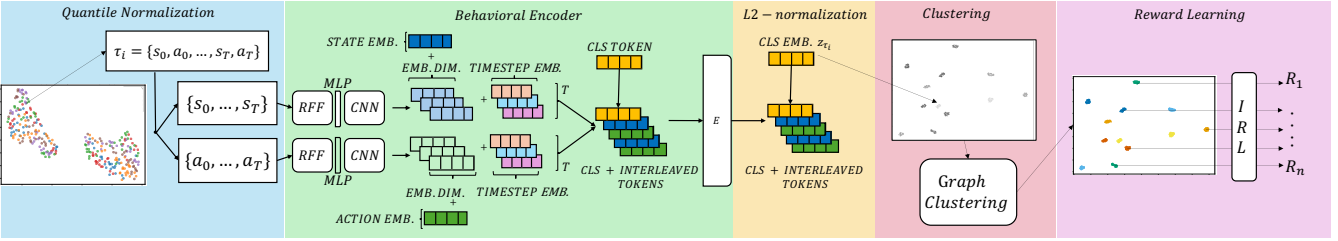


Figure 1: **CoMI-IRL pipeline.** States and actions of each quantile normalized input trajectory τ_i pass through a Random Fourier Feature (RFF) encoding with Gaussian mapping, a shallow *MLP* and a 1D *CNN* layer. After adding timestep and modality embeddings (distinguishing states and actions), we interleave the two sequences and prepend a *CLS* token summarizing the trajectory. On the resulting embeddings, we apply graph-clustering to get cluster labels and apply IRL independently on each cluster.

MLP and a 1D *CNN*, to capture short-range temporal patterns in the trajectory. The *RFF* encoding overcomes known *MLP* spectral bias towards low-frequency functions by injecting a rich set of sinusoidal features at multiple random orientation and frequencies. Each block’s output is enriched with a timestep (used as positional encoding) and either a state or action embedding to further differentiate.

Next, we interleave them to recreate the single input sequence. We prepend a *CLS* token to this sequence that will function as the trajectory summary. The resulting sequence is then passed through the encoder to capture the trajectory’s global dependencies, summarized in the *CLS* embedding, which for simplicity we name z_{τ_i} . Finally, we L2-normalize the *CLS* token of the encoder’s output, restricting the output space to the unit hypersphere [Wang and Isola, 2020].

Contrastive Framework and Loss Function

As we aim to learn a discriminative representation z_{τ_i} of each input trajectory τ_i , we apply the symmetric InfoNCE loss at multiple granularity levels, with DIM included as a regularization term (cf. Section 2.2).

First, we generate two dropout-augmented views of each input τ_i : $z_{\tau_i}^1$ and $z_{\tau_i}^2$, forming a positive pair. This maps similar trajectories close together in the embedding space, allowing for the emergence of areas with distinct behavioral modes. This loss component is defined as:

$$\mathcal{L}_{\text{CLS}} = \frac{1}{2N} \sum_{i=1}^{2N} \ell_{\text{InfoNCE}}(z_{\tau_i}^1, z_{\tau_i}^2). \quad (3)$$

with N being the number of trajectories in the batch.

Second, we sample n segments of length L , with starting point $q \in \{0, T - L\}$ from each input trajectory. Each segment is defined as $\tau_i(q, L) = \{s_q, a_q, \dots, s_{q+L}, a_{q+L}\}$, and passed through the encoder to create n segment embeddings $z_{\tau_i(q, L)}^k$. Aiming to promote consistency between local (segment-level) and trajectory representations, we apply InfoNCE between each trajectory embeddings and its segment embeddings. This loss component, \mathcal{L}_{SEG} , performs the same operation as Equation 3, but applied between z_{τ_i} and $z_{\tau_i(q, L)}^k$. To push representations even closer together in each area, we apply InfoNCE between all unique pairs of segment embed-

dings:

$$\mathcal{L}_{\text{PAIR}} = \frac{1}{\binom{n}{2}} \sum_{k=1}^{n-1} \sum_{j=k+1}^n \ell_{\text{InfoNCE}}(z_{\tau_i(q, L)}^k, z_{\tau_i(q, L)}^j). \quad (4)$$

We also add a DIM component to the loss, \mathcal{L}_{DIM} , which follows Equation 2, with the goal of keeping local structure consistent and further stabilize representations. This component explicitly maximize the mutual information between trajectory representations and their local features without forcing token-level separation across trajectories.

Combining the components, we get our complete loss:

$$\mathcal{L} = \alpha \mathcal{L}_{\text{CLS}} + \beta \mathcal{L}_{\text{DIM}} + \gamma \mathcal{L}_{\text{SEG}} + \delta \mathcal{L}_{\text{PAIR}} \quad (5)$$

where α, β, γ and δ are balancing coefficients.

3.2 Clustering and Reward Learning

In principle, any clustering method not requiring K^* could be used. However, density-based methods such as HDBSCAN [Campello *et al.*, 2013] can be highly sensitive to hyperparameters, require clear density gaps (not often available in continuous manifolds), and its adaptation relies on the fixed density structure of the original tree. Therefore, we cluster the embeddings using a graph-based community detection approach not requiring K^* via local connectivity. We construct a weighted k -nearest neighbor graph over trajectory embeddings, where nodes represent trajectories and edge weights are defined by cosine similarity between embedding. This choice is motivated by the fact that our contrastive objective optimizes for directional alignment. Rather than assuming a fixed global scale, we analyze the connectivity structure of the graph to identify stable behavioral partitions. In cases where the graph decomposes into multiple connected components, these components directly define clusters. If the graph remains fully connected, we apply community detection using the Leiden algorithm [Traag *et al.*, 2018] to identify coherent subgraphs by optimizing modularity. Graph parameters are selected based on clustering stability across resolution levels, avoiding reliance on external clustering objectives or prior assumptions about the number of modes k .

We augment graph edge weights with trajectory-level Jacobian features estimated through finite differences, as they showed low correlation with the embeddings (detailed in the Supplementary Material). Incorporating Jacobian similarity

preserves the decoupling from reward learning, while helping separate distinct behavioral patterns. This is especially useful in embedding spaces with a continuous manifold structure, where embedding similarity alone may be insufficient to separate closely related behaviors. These statistical features summarize average local state-action sensitivities along each trajectory and aim to capture behavioral dynamics independently of reward structure or task specification.

For each discovered cluster, we independently apply a single-intention IRL algorithm (we test our framework with deep learning based methods to allow non-linear reward functions) to learn a reward function for each cluster. This decoupling allows reward learning to operate on semantically coherent behaviors identified purely from behavioral similarity.

3.3 Adaptation to new behaviors

When unseen trajectories arrive, CoMI-IRL adapts through encoder finetuning followed by two-stage clustering to handle embedding drift.

Encoder Finetuning

To incorporate unseen behaviors and limit catastrophic forgetting, we restructure the embedding space to map new trajectories while preserving the geometry induced by past data. This is done by finetuning the BE on the old and new data with the addition of a stability regularizer to limit the latent drift of the learned structure. Specifically, we adopt a *less-forget constraint* [Hou *et al.*, 2019] loss, which preserves the geometric configuration by fixing the original embeddings and computing a novel distillation loss on the new embeddings. This regularizer implicitly implements rehearsal by revisiting previously observed trajectories during finetuning.

Formally, let b_i be the L2-normalized embedding of a rehearsed sample generated by the frozen (reference) encoder, and let a_i be the corresponding embedding produced by the finetuned encoder. The stability loss is defined as: $\mathcal{L}_{\text{stab}} = \frac{1}{N} \sum_{i=1}^N (1 - a_i^\top b_i)$. This loss encourages new embeddings to align with the orientation of the original representation by penalizing cosine dissimilarity.

Finetuned Clustering and New Reward Learning

Despite stability regularization, finetuning inevitably causes some embedding drift that invalidates original cluster assignments computed in the pre-finetuning space. We address this with a two-stage clustering procedure (further detailed in Supplementary Material): First, we re-cluster only the seen data leveraging the known expected cluster count K_{baseline} from the baseline space. The algorithm prioritizes configurations producing exactly K_{baseline} clusters, yielding recovered centroids and radii that represent baseline modes in the new embedding space. Online trajectories within a novelty threshold θ of any recovered centroid are assigned to that cluster; those outside all radii are marked as novel candidates. Novel candidates are then sub-clustered via connected component analysis or Leiden clustering, following the same process described in Section 3.2. This yields a partition where recovered clusters retain their baseline agents, while novel clusters trigger the training of new policies.

4 Experiments

In our experiments, we first analyze how the relationship between the assumed (K) and true (K^*) number of behavioral modes (i.e., $K \neq K^*, K = K^*$) impacts clustering and reward learning. Second, we visualize the embedding space and analyze the dataset as partitioned by our model. Finally, we test the adaptability of our approach to new behaviors.

We include as main baseline Ess-InfoGAIL [Fu *et al.*, 2023], which requires a small amount of labeled data and K fixed a priori. Ess-InfoGAIL represents one of the current state-of-the-art entangled methods for MI-IRL. While methods inferring K exist, they are often not computationally feasible on continuous spaces (cf. Section 5). We also include baselines combining different clustering algorithms (K-Means [Lloyd, 1982; MacQueen, 1967], and our graph-based clustering) as versions of our approach without contrastive embeddings, some requiring a fixed number of clusters K and others inferring it. We test CoMI-IRL and each of the baseline methods using with Generative Adversarial Imitation Learning (GAIL) [Ho and Ermon, 2016] and Adversarial IRL (AIRL) [Fu *et al.*, 2017] as reward learning algorithm, with an exception for Ess-InfoGAIL, as it is based on GAIL and not easily transferable to AIRL.

We deploy all methods on three MuJoCo environments: Reacher-v4, Pusher-v4 and Walker2D-v4. All environments follow the objectives and setups used in [Fu *et al.*, 2023]. For each environment, we pre-train K^* expert policies, each corresponding to K^* different behavior modes, and for each policy we sample a set of 100 expert demonstrations.

We test all approaches over three seeds, reporting the clustering performance through Normalized Mutual Information (NMI) [Xu *et al.*, 2003], Adjusted Rand Index (ARI) [Rand, 1971], Silhouette Score (Sil) [Rousseeuw, 1987], and the reward learning performance through Average Task Reward (ATR) [Fu *et al.*, 2023]. NMI quantifies the correlation between two clusterings (in this case, the ground truth and the result of the clustering phase), while ARI measures their similarity. Both assume values between 0 and 1, with a higher value indicating a better performance. Sil measures how well-separated and distinct clusters are in an unsupervised clustering analysis, and ranges from -1 to 1 . To calculate the ATR of each method in each specific environment, we generate 100 rollouts for each behavioral mode using each of the considered methods, and we normalize all the results related to the expert policy, meaning that an ATR of 1 corresponds to the learned policy behaving as well as the expert one. The configurations used for each experiment and for each method are available in the Supplementary Material.

4.1 Clustering and Reward Analysis

In this experiment, we show how the relationship between K and K^* impacts clustering and reward learning. Ess-InfoGAIL and KMeans-based baselines(K-GAIL/AIRL) require fixed K , while the Graph-based baseline (G-GAIL/AIRL) and CoMI-IRL infer it from data. The clustering quality and reward learning performance of all methods in all tested conditions are presented in Table 1. As Ess-InfoGAIL requires a small subset of labeled demonstrations (1% of the unlabeled demonstrations) for each behav-

ioral mode, in the $K < K^*$ case we are simulating a scenario in which the labeling underspecifies the number of latent behaviors. To do so, we remove the labeled trajectories for three modes out of six, but we keep the entire unlabeled dataset. For $K > K^*$ case, we duplicate the labeled trajectories, mimicking an overspecification in the number of latent behaviors. For all conditions, we test the performance on the number of clusters, either fixed or inferred based on the method.

Table 1: **Performance Overview.** Clustering quality (NMI, ARI, Sil) and reward learning (ATR). For inferred methods, the column K shows the amount of inferred clusters. Best results are bolded, and an asterisk * indicates cases of mode collapse.

Method	K	Clustering Quality			Reward
		NMI	ARI	Sil	
Reacher-v4 ($K^* = 6$)					
K-GAIL	3	0.14 \pm 0.01	0.08 \pm 0.01	0.09 \pm 0.00	0.31 \pm 0.07
	6	0.41 \pm 0.04	0.24 \pm 0.02	0.08 \pm 0.00	0.31 \pm 0.15
	12	0.41 \pm 0.01	0.22 \pm 0.02	0.08 \pm 0.00	0.81 \pm 0.37
K-AIRL	3	0.14 \pm 0.01	0.08 \pm 0.01	0.09 \pm 0.00	0.31 \pm 0.04
	6	0.41 \pm 0.04	0.24 \pm 0.02	0.08 \pm 0.00	0.32 \pm 0.16
	12	0.41 \pm 0.01	0.22 \pm 0.02	0.08 \pm 0.00	0.80 \pm 0.37
Ess-InfoGAIL	3	0.35 \pm 0.05	0.36 \pm 0.05	0.06 \pm 0.01	0.40 \pm 0.17
	6	0.55 \pm 0.05	0.49 \pm 0.07	0.03 \pm 0.01	0.45 \pm 0.22
	12	0.37 \pm 0.02	0.20 \pm 0.01	-0.04 \pm 0.04	0.97\pm0.75
G-GAIL	2	0.01 \pm 0.00	0.00 \pm 0.00	0.12 \pm 0.00	0.23 \pm 0.02
G-AIRL	2	0.01 \pm 0.00	0.00 \pm 0.00	0.12 \pm 0.00	0.26 \pm 0.02
CoMI-IRL(GAIL)	12	0.84 \pm 0.00	0.63 \pm 0.00	0.87 \pm 0.06	0.96 \pm 0.13
CoMI-IRL(AIRL)	12	0.84 \pm 0.00	0.63 \pm 0.00	0.87 \pm 0.06	0.94 \pm 0.11
Pusher-v4 ($K^* = 6$)					
K-GAIL	3	0.72 \pm 0.00	0.48 \pm 0.00	0.16 \pm 0.00	0.14 \pm 0.29
	6	1.00 \pm 0.00	1.00 \pm 0.00	0.15 \pm 0.00	0.77 \pm 0.41
	12	0.87 \pm 0.01	0.74 \pm 0.05	0.06 \pm 0.01	0.76 \pm 0.38
K-AIRL	3	0.72 \pm 0.00	0.48 \pm 0.00	0.16 \pm 0.00	1.0 \pm 0.21
	6	1.00 \pm 0.00	1.00 \pm 0.00	0.15 \pm 0.00	1.10 \pm 0.11
	12	0.87 \pm 0.01	0.74 \pm 0.05	0.06 \pm 0.01	1.09 \pm 0.12
Ess-InfoGAIL	3	0.77 \pm 0.04	0.73 \pm 0.06	0.39 \pm 0.10	0.45 \pm 0.31
	6	0.90 \pm 0.02	0.75 \pm 0.03	0.44 \pm 0.04	0.77 \pm 0.23
	12	0.61 \pm 0.09	0.32 \pm 0.07	0.16 \pm 0.04	0.37 \pm 0.16
G-GAIL	6	1.00 \pm 0.00	1.00 \pm 0.00	0.15 \pm 0.00	0.77 \pm 0.43
G-AIRL	6	1.00 \pm 0.00	1.00 \pm 0.00	0.15 \pm 0.00	1.10 \pm 0.11
CoMI-IRL(GAIL)	6	1.00 \pm 0.00	1.00 \pm 0.00	0.99 \pm 0.01	0.77 \pm 0.41
CoMI-IRL(AIRL)	6	1.00 \pm 0.00	1.00 \pm 0.00	0.99 \pm 0.01	1.10 \pm 0.11
Walker2D-v4 ($K^* = 3$)					
K-GAIL	3	0.52 \pm 0.02	0.46 \pm 0.06	0.06 \pm 0.02	0.57 \pm 0.43
	6	0.44 \pm 0.03	0.30 \pm 0.01	0.05 \pm 0.01	1.58\pm2.77*
	12	0.46 \pm 0.02	0.31 \pm 0.01	0.01 \pm 0.02	1.20\pm1.26*
K-AIRL	3	0.52 \pm 0.02	0.46 \pm 0.06	0.06 \pm 0.02	0.32 \pm 0.59
	6	0.44 \pm 0.03	0.30 \pm 0.01	0.05 \pm 0.01	0.61 \pm 0.51
	12	0.46 \pm 0.02	0.31 \pm 0.01	0.01 \pm 0.02	0.42 \pm 0.53
Ess-InfoGAIL	3	0.44 \pm 0.03	0.38 \pm 0.03	0.10 \pm 0.08	0.49 \pm 0.38
	6	0.29 \pm 0.06	0.21 \pm 0.06	-0.01 \pm 0.02	0.69\pm1.33*
	12	0.35 \pm 0.05	0.16 \pm 0.06	-0.05 \pm 0.04	0.42 \pm 0.73
G-GAIL	2	0.50 \pm 0.00	0.45 \pm 0.00	0.09 \pm 0.00	0.39 \pm 0.46
G-AIRL	2	0.50 \pm 0.00	0.45 \pm 0.00	0.09 \pm 0.00	0.47 \pm 0.41
CoMI-IRL(GAIL)	3.3 \pm 0.47	0.75 \pm 0.05	0.77 \pm 0.07	0.60 \pm 0.01	0.38 \pm 0.57
CoMI-IRL(AIRL)	3.3 \pm 0.47	0.75 \pm 0.05	0.77 \pm 0.07	0.60 \pm 0.01	0.64 \pm 0.57

The results show how, without the embeddings, decoupling can lead to high performance in case of $K = K^*$ and clearly separable behavioral modes (such as in the Pusher case, where K-Means and Graph clustering with $K=6$ have perfect NMI/ARI, with the GAIL based models achieving ATR comparable with Ess-InfoGAIL). When trajectories are not

clearly separable or $K \neq K^*$, clustering performance drops. This degrades the reward learning, causing mode collapse in certain Walker cases using GAIL. CoMI-IRL, by restructuring the space, outperforms the baselines both in clustering and reward learning. On Walker, it finds an additional small cluster in one case. In the Pusher case, the AIRL-based methods outperform the GAIL-based ones and the expert, reaching an ATR of 1.10 ± 0.11 due AIRL's recovery of an explicit reward function which is more robust in case of mixed clusters.

In the $K < K^*$ case, Ess-InfoGAIL is forced to explain all K^* behavioral modes with K latent codes, meaning that trajectories from other behavioral modes in the dataset will contaminate the training of the K considered classes, as it shows with a low NMI and ATR. In the $K > K^*$ case, it is forced to use all latent codes even if the dataset does not require all the modes, also leading to a lower NMI. Interestingly, the ATR in the Reacher environment is higher for $K=12$ than for $K=6$ case for most methods, with Ess-InfoGAIL showing high instability (0.97 ± 0.75) against CoMI-IRL's comparable performances with significantly lower variance 0.96 ± 0.13 and 0.94 ± 0.11 . As CoMI-IRL also finds $K=12$ classes, it suggests that the K^* pre-trained expert policies actually produced a finer-grained behavioral structure with twelve different behavioral modes, and we investigate this further.

4.2 Behavior Visualization

In Figure 2, for each environment, we visualize the original space of trajectories and the respective embedding space built by the BE. For both, we use UMAP [McInnes *et al.*, 2018] as it preserves more of the global structure of the space. By visualizing the embeddings produced by the BE, it is possible to analyze how behaviors relate to each other without introducing any assumption in terms of reward.

In Pusher, the trajectories are already fairly separable, explaining K-GAIL and G-GAIL perfect clustering performance when $K = K^*$. Ess-InfoGAIL approaches the task from a reward-likelihood angle and does not consider the inherit similarity between trajectories as CoMI-IRL does. As a result, Ess-InfoGAIL does not manage to perfectly disentangle the modes, highlighting an advantage of the decoupling.

In Reacher, our model notably detects double the amount of true behavioral clusters (twelve instead of six). To further investigate this finer-grained behavioral structure, we analyzed the geometric composition of the dataset as partitioned by our method. This analysis revealed that our method successfully disentangled the behavioral modes, creating clusters that are consistent with respect to the configuration of the elbow joint angle (positive or negative), shown in Table 2. We evaluate how the trained policies perform in terms of the elbow angle. We generate 50 rollouts for each agent and we analyze the angle consistency. The results are reported in Table 3. CoMI-IRL achieves low variance across all modes, consistently identifying one “Up” and one “Down” agent per mode, allowing for controllability. Ess-InfoGAIL exhibits high variance for Mode 1 (± 0.52 rad), indicating that the latent code fails to capture a consistent physical strategy across seeds. In the other modes the model shows consistency, however this also means that it does not allow for selection of a preferred elbow configuration, collapsing into one configura-

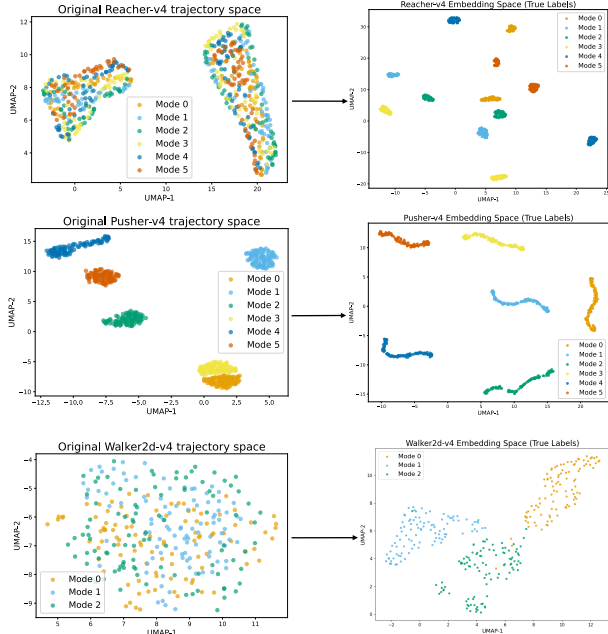


Figure 2: 2D UMAP visualizations of the original trajectory space of each environment (from top to bottom: Reacher, Pusher, Walker2D), and the respective embedding space resulting from the BE.

tion per mode. Looking at the MI-IRL task from a behavior-first perspective offers a level of nuance interpretability and controllability not captured by the expert definition of K and that entangled models such as Ess-InfoGAIL don't allow due to the latent code structuring. Ablation experiments (see in the Supplementary Material) support DIM (cf. Section 2) as a regularization term and confirm the pre-processing block as a crucial component on overlapping spaces, highlighting the segment and pairwise losses as key loss components.

Table 2: **Disentanglement of elbow angle.** CoMI-IRL splits each target mode into two distinct strategy clusters: “Elbow-Down” ($\theta < 0$) and “Elbow-Up” ($\theta > 0$). Values are in radians (Mean \pm SD).

Mode	Elbow-Down		Elbow-Up	
	ID	θ	ID	θ
0	C8	-0.92 ± 0.14	C4	$+1.96 \pm 0.30$
1	C7	-0.77 ± 0.19	C5	$+1.30 \pm 0.24$
2	C10	-1.18 ± 0.31	C6	$+0.80 \pm 0.19$
3	C11	-1.99 ± 0.24	C2	$+0.90 \pm 0.20$
4	C9	-2.08 ± 0.18	C1	$+1.62 \pm 0.24$
5	C0	-1.63 ± 0.20	C3	$+2.16 \pm 0.22$

4.3 Adaptation to new behaviors

In this experiment, we evaluate CoMI-IRL's adaptability to new behaviors. Entangled methods cannot adapt to unseen behaviors without full retraining. We consider the case of an initial dataset containing $K_{\text{base}} = K^*/2$ behavioral modes, with the other half received at a later moment. We hereby show how CoMI-IRL does not need to retrain the entire

Table 3: **Strategy Consistency.** Comparison of learned elbow angles (θ in radians, Mean \pm SD). CoMI-IRL consistently identifies two distinct strategies per mode, whereas Ess-InfoGAIL collapses them, leading to high variance (e.g., Mode 1).

Mode	CoMI-IRL (Ours)		Ess-InfoGAIL
	Down (θ)	Up (θ)	Angle (θ)
0	-0.85 ± 0.02	$+1.79 \pm 0.04$	$+1.90 \pm 0.03$
1	-0.71 ± 0.03	$+1.15 \pm 0.03$	$+0.21 \pm 0.52$
2	-1.09 ± 0.01	$+0.71 \pm 0.01$	-0.18 ± 0.18
3	-1.82 ± 0.05	$+0.84 \pm 0.02$	-1.86 ± 0.06
4	-2.02 ± 0.04	$+1.51 \pm 0.07$	-1.89 ± 0.17
5	-1.54 ± 0.06	$+1.95 \pm 0.08$	$+1.94 \pm 0.04$

framework, but it is adaptable to unseen behaviors and maintains previously learned knowledge. For Reacher and Pusher, we remove half of the modes from the original dataset, apply CoMI-IRL for the remaining ones, and then finetune adding the new behaviors. For Walker-2D, which has only three modes, we remove the third mode. We report NMI, ARI, Silhouette and ATR for K_{base} and $K_{\text{finetuned}}$ in Table 4.

Table 4: **Adaptation Performance.** NMI, ARI, Silhouette, and ATR scores before (K_{base}) and after ($K_{\text{finetuned}}$) adapting to unseen behaviors. K^* denotes the total number of modes in the final dataset and \hat{K} the number of inferred ones.

Stage	NMI	ARI	Sil	ATR	\hat{K}
Reacher-v4 ($K^* = 6$)					
K_{base}	0.76 ± 0.00	0.57 ± 0.00	0.85 ± 0.00	0.93 ± 0.11	6 ± 0.00
$K_{\text{finetuned}}$	0.84 ± 0.00	0.63 ± 0.00	0.81 ± 0.00	0.93 ± 0.10	12 ± 0.00
Pusher-v4 ($K^* = 6$)					
K_{base}	1.00 ± 0.00	1.00 ± 0.00	0.76 ± 0.00	1.10 ± 0.14	3 ± 0.00
$K_{\text{finetuned}}$	1.00 ± 0.00	1.00 ± 0.00	0.76 ± 0.00	1.09 ± 0.12	6 ± 0.00
Walker2D-v4 ($K^* = 3$)					
K_{base}	0.98 ± 0.02	0.99 ± 0.01	0.54 ± 0.05	0.57 ± 0.31	2 ± 0.00
$K_{\text{finetuned}}$	0.90 ± 0.01	0.88 ± 0.01	0.25 ± 0.04	0.87 ± 0.62	4 ± 0.00

The results show how CoMI-IRL adapts to new behaviors through finetuning. In the first two environments, CoMI-IRL manages to maintain performance between stages and to correctly identify K . On Walker-2D, NMI/ARI are high on K_{base} as the first two modes (moving forward or backward) are separable. The two-stage clustering allows the model to more selectively isolate novel trajectories, leading to higher NMI/ARI and ATR on $K_{\text{finetuned}}$ compared to the full dataset experiment of Table 1, while oversegmenting the new mode.

5 Related Work

EM-based approaches Early parametric EM-based approaches [Babes *et al.*, 2011; Snoswell *et al.*, 2021; Ramponi *et al.*, 2020] typically require knowledge of K and model the reward function as a linear combination of handcrafted features [Ng and Russell, 2000; Levine *et al.*, 2010], and the performance highly depends on the how well these are selected [Choi and Kim, 2013]. In CoMI-IRL, as in other deep MI-IRL methods, we do not need to handcraft features.

Nonparametric Bayesian approaches When K is unknown, it can be inferred through Bayesian solutions [Choi and Kim, 2012; Bighashdel *et al.*, 2021], with some works learning the reward more flexibly through Gaussian Process kernels [Levine *et al.*, 2011] or deep learning [Bighashdel *et al.*, 2021]. However, this comes at the cost of a significantly larger overhead and computational costs [Ramonpi *et al.*, 2020]. The application in continuous state-action spaces as the ones considered in our work is sparsely addressed in literature [Almingol and Montesano, 2015; Rajasekaran *et al.*, 2017] due to the computational limitations of applying Bayesian methods in such spaces. In CoMI-IRL, we work specifically on continuous state-action spaces, where the application of current methods in this line area is limited.

Deep Generative MI-IRL Methods Deep Generative MI-IRL methods transfer the IRL problem to multi-expert settings by learning multiple rewards, often via latent conditioning. Different methods extend GAIL with MI maximization between trajectories and latent codes c , enabling mode separation without explicit clustering [Li *et al.*, 2017; Hausman *et al.*, 2017; Fu *et al.*, 2023]. However, maximizing a lower bound on MI in these works depends on the generator’s ability to cover the distribution. If the policy fails to capture a specific mode, the clustering signal degrades. In contrast, CoMI-IRL’s decoupled design employs a discriminative objective that optimizes the embedding geometry for separability, independent of the policy’s performance.

Likelihood Connection The mentioned approaches cluster trajectories via likelihood-based mechanisms: in EM-based methods, it is the likelihood of a trajectory being generated by a certain reward function; Bayesian solutions cluster via posterior inference over the components of the mixture model; and generative approaches cluster through the probability of generation from a conditioned policy. A connection between likelihood-based and generative-based approaches in IRL was established by [Finn *et al.*, 2016], which persists in the multi-intention case. In contrast, CoMI-IRL clusters via contrastive embedding similarity.

Trajectory Embedding Methods The use of sequence models and contrastive techniques to learn trajectory embeddings gathered a lot of attention in recent works. [Vivekanandan *et al.*, 2025] employ Transformer encoders with triplet losses on spatially augmented short trajectories to learn motion priors for forecasting. TrajCL [Chang *et al.*, 2023] employs dual-feature (spatial/structural) self-attention Transformers with contrastive augmentations (shifting/masking) for similarity queries, focusing on spatial ranking without intention handling. [Kujanpää *et al.*, 2025] proposes Discrete Style Diffusion Policy (DSDP) as a Behavioral Cloning method, combining InfoNCE with Lookup-Free Quantization (LFQ) to extract discrete styles on sub-trajectories for conditional diffusion behavior cloning, tying embeddings to generation rather than reward inference. [Ge *et al.*, 2025] introduce Variational Trajectory Embeddings (VTE), a method designed to capture a continuous ability vector representing a trajectory’s proficiency on a single task. In VTE, first a probabilistic skill extractor (based on a Hierarchical State Space Model and the Learning Options via Compression

(LOVE) [Jiang *et al.*, 2022] framework) processes a trajectory to yield a sequence of latent skill distributions. Secondly, a transformer-based Variational Autoencoder (VAE) gets this skill sequence in input to compute final embedding’s posterior. The model is trained to maximize the VAE’s Evidence Lower Bound (ELBO), pairing a KL divergence regularizer and an action reconstruction loss, where a policy conditioned on the embedding must replicate the trajectory’s actions.

In contrast with VTE’s variational approach, which relies on intermediate skill representations and a reconstruction objective to model how a single task is performed, CoMI-IRL learns directly from raw state-action sequences using a purely contrastive objective. Its goal is to learn a discriminative embedding space for behavioral clustering, enabling a fully decoupled and adaptive MI-IRL method.

6 Limitations & Future Work

While results are encouraging, there are limitations. CoMI-IRL suffers from known Transformers limitations [Sanford *et al.*, 2023], relying on the learned space quality and hyperparameter choice. However, visualizing the embedding space allows for a qualitative analysis of the results before the IRL phase. The clustering algorithm also plays a determinant role, and our method automatically finds a stable structure for the space considered. A deeper analysis of the Jacobian edge reweighting hyperparameters is part of future studies. While CoMI-IRL has been shown to adapt, future work includes a deeper study on the scalability to multiple modes and the robustness to catastrophic forgetting. The stability regularizer with rehearsal mechanism and the structural isolation given by the decoupling suggest a good degree of robustness, but further work is needed. Other future directions include the reward learning phase, taking into account the connection between clusters representing different ways of achieving the same task. Finally, interpretability results need to be assessed on a user study with real-world data, as real-world scenarios might have more subtle differences. This could also be explored in combination with potentially introducing human feedback in the process, to study the alignment between demonstrated behavioral modes and stated intentions.

7 Conclusions

We presented CoMI-IRL, a transformer-based unsupervised framework for MI-IRL decoupling behavior clustering from reward learning: it first learns trajectory embeddings, clusters them, and then applies single-reward IRL to each discovered cluster. In our experiments on the MuJoCo benchmark, CoMI-IRL produced better clustering performance and downstream policy performance compared to the baseline. We analyzed how the relationship between K and K^* impacts existing methods, while our approach infers K from data and shows adaptability to unseen behaviors. Decoupling also allowed us to analyze the dataset as partitioned by our model in terms of behavioral similarity and not through the learned rewards, facilitating the interpretation of similarities in the dataset. In doing so, we enhance the applicability of MI-IRL solutions to dynamic scenarios, contributing to broader integration of adaptable AI systems in the real world.

References

[Abbeel and Ng, 2004] Pieter Abbeel and Andrew Y. Ng. Apprenticeship learning via inverse reinforcement learning. In *Proc. of ICML*, volume 69 of *ACM International Conference Proceeding Series*, 2004.

[Almingol and Montesano, 2015] Javier Almingol and Luis Montesano. Learning multiple behaviours using hierarchical clustering of rewards. In *2015 IEEE/RSJ Int. Conf. on Intelligent Robots and Systems (IROS)*, pages 4608–4613, 2015.

[Babes *et al.*, 2011] Monica Babes, Vukosi N. Marivate, et al. Apprenticeship learning about multiple intentions. In *Proc. of ICML*, pages 897–904, 2011.

[Bighashdel *et al.*, 2021] Ariyan Bighashdel, Panagiotis Meletis, et al. Deep adaptive multi-intention inverse reinforcement learning. In *Proc. PKDD*, volume, volume 12975 of *LNCS*, pages 206–221, 2021.

[Bighashdel *et al.*, 2023] Ariyan Bighashdel, Pavol Jancura, and Gijs Dubbelman. Model-free inverse reinforcement learning with multi-intention, unlabeled, and overlapping demonstrations. *Mach. Learn.*, 112(7):2263–2296, 2023.

[Bolstad *et al.*, 2003] Benjamin M Bolstad, Rafael A Irizarry, et al. A comparison of normalization methods for high density oligonucleotide array data based on variance and bias. *Bioinformatics*, 19(2):185–193, 2003.

[Campello *et al.*, 2013] Ricardo JGB Campello, Davoud Moulavi, and Jörg Sander. Density-based clustering based on hierarchical density estimates. In *Proc. PAKDD*, pages 160–172, 2013.

[Chang *et al.*, 2023] Yanchuan Chang, Jianzhong Qi, et al. Contrastive trajectory similarity learning with dual-feature attention. In *2023 IEEE 39th Int. Conf. on data engineering (ICDE)*, pages 2933–2945. IEEE, 2023.

[Chen *et al.*, 2020] Ting Chen, Simon Kornblith, et al. A simple framework for contrastive learning of visual representations. In *Proc. of ICML*, volume 119 of *Proceedings of Machine Learning Research*, pages 1597–1607, 2020.

[Chen *et al.*, 2021] Lili Chen, Kevin Lu, et al. Decision transformer: Reinforcement learning via sequence modeling. In *Adv. Neural Inf. Process. Syst. (NIPS)*, pages 15084–15097, 2021.

[Choi and Kim, 2012] Jaedeug Choi and Kee-Eung Kim. Nonparametric bayesian inverse reinforcement learning for multiple reward functions. In *Adv. Neural Inf. Process. Syst. (NIPS)*, pages 314–322, 2012.

[Choi and Kim, 2013] Jaedeug Choi and Kee-Eung Kim. Bayesian nonparametric feature construction for inverse reinforcement learning. In *Proc. IJCAI*, pages 1287–1293, 2013.

[Deng *et al.*, 2023] Xiaozhi Deng, Dong Huang, et al. Strongly augmented contrastive clustering. *Pattern Recognition*, 139:109470, 2023.

[Devlin *et al.*, 2019] Jacob Devlin, Ming-Wei Chang, et al. BERT: Pre-training of deep bidirectional transformers for language understanding. In *Proc. of NAACL-HLT*, pages 4171–4186, Minneapolis, Minnesota, 2019.

[Finn *et al.*, 2016] Chelsea Finn, Paul Christiano, et al. A connection between generative adversarial networks, inverse reinforcement learning, and energy-based models. *Corr*, 2016.

[Fu *et al.*, 2017] Justin Fu, Katie Luo, and Sergey Levine. Learning robust rewards with adversarial inverse reinforcement learning. *ArXiv preprint*, abs/1710.11248, 2017.

[Fu *et al.*, 2023] Huiqiao Fu, Kaiqiang Tang, et al. Ess-infogail: Semi-supervised imitation learning from imbalanced demonstrations. In *Adv. Neural Inf. Process. Syst. (NIPS)*, 2023.

[Gao *et al.*, 2021] Tianyu Gao, Xingcheng Yao, and Danqi Chen. SimCSE: Simple contrastive learning of sentence embeddings. In *Proc. of EMNLP*, pages 6894–6910, Online and Punta Cana, Dominican Republic, 2021.

[Ge *et al.*, 2025] Zichang Ge, Changyu Chen, et al. On learning informative trajectory embeddings for imitation, classification and regression. 2025.

[Gleave *et al.*, 2022] Adam Gleave, Mohammad Tafeeque, et al. imitation: Clean imitation learning implementations, 2022.

[Hausman *et al.*, 2017] Karol Hausman, Yevgen Chebotar, et al. Multi-modal imitation learning from unstructured demonstrations using generative adversarial nets. In *Adv. Neural Inf. Process. Syst. (NIPS)*, pages 1235–1245, 2017.

[Hjelm *et al.*, 2019] R. Devon Hjelm, Alex Fedorov, et al. Learning deep representations by mutual information estimation and maximization. In *Proc. of ICLR*, 2019.

[Ho and Ermon, 2016] Jonathan Ho and Stefano Ermon. Generative adversarial imitation learning. In *Adv. Neural Inf. Process. Syst. (NIPS)*, pages 4565–4573, 2016.

[Hou *et al.*, 2019] Saihui Hou, Xinyu Pan, et al. Learning a unified classifier incrementally via rebalancing. In *IEEE Conference on CVPR*, pages 831–839, 2019.

[Jiang *et al.*, 2022] Yiding Jiang, Evan Zheran Liu, et al. Learning options via compression. In *Adv. Neural Inf. Process. Syst. (NIPS)*, 2022.

[Kujanpää *et al.*, 2025] Kalle Kujanpää, Daulet Baimukashov, et al. Discrete contrastive learning for diffusion policies in autonomous driving. 2025.

[Levine *et al.*, 2010] Sergey Levine, Zoran Popovic, and Vladlen Koltun. Feature construction for inverse reinforcement learning. In *Adv. Neural Inf. Process. Syst. (NIPS)*, pages 1342–1350, 2010.

[Levine *et al.*, 2011] Sergey Levine, Zoran Popovic, and Vladlen Koltun. Nonlinear inverse reinforcement learning with gaussian processes. In *Adv. Neural Inf. Process. Syst. (NIPS)*, pages 19–27, 2011.

[Li *et al.*, 2017] Yunzhu Li, Jiaming Song, and Stefano Ermon. Infogail: Interpretable imitation learning from visual

demonstrations. In *Adv. Neural Inf. Process. Syst. (NIPS)*, pages 3812–3822, 2017.

[Li *et al.*, 2021] Yang Li, Si Si, et al. Learnable fourier features for multi-dimensional spatial positional encoding. In *Adv. Neural Inf. Process. Syst. (NIPS)*, pages 15816–15829, 2021.

[Lloyd, 1982] Stuart Lloyd. Least squares quantization in pcm. *IEEE trans.s on information theory*, 28(2):129–137, 1982.

[MacQueen, 1967] J MacQueen. Multivariate observations. In *Proc. of the 5th Berkeley Symposium on Mathematical Statistics and Probability*, volume 1, pages 281–297, 1967.

[McInnes *et al.*, 2018] Leland McInnes, John Healy, and James Melville. Umap: Uniform manifold approximation and projection for dimension reduction. 2018.

[Michini and How, 2012] Bernard Michini and Jonathan P. How. Bayesian nonparametric inverse reinforcement learning. In *Proc ECML PKDD*, volume 7524 of *Lecture Notes in Computer Science*, pages 148–163, 2012.

[Ng and Russell, 2000] Andrew Y. Ng and Stuart J. Russell. Algorithms for inverse reinforcement learning. In *Proc. of ICML*, pages 663–670, 2000.

[Oord *et al.*, 2018] Aaron van den Oord, Yazhe Li, and Oriol Vinyals. Representation learning with contrastive predictive coding. 2018.

[Qin *et al.*, 2023] Guanghui Qin, Yukun Feng, and Benjamin Van Durme. The NLP task effectiveness of long-range transformers. In *Proceedings of European Chapter of the ACL*, pages 3774–3790, Dubrovnik, Croatia, 2023.

[Raffin *et al.*, 2021] Antonin Raffin, Ashley Hill, et al. Stable-baselines3: Reliable reinforcement learning implementations. *J. Mach. Learn. Res.*, 22:268:1–268:8, 2021.

[Rahaman *et al.*, 2019] Nasim Rahaman, Aristide Baratin, et al. On the spectral bias of neural networks. In *Proc. of ICML*, volume 97 of *Proceedings of Machine Learning Research*, pages 5301–5310, 2019.

[Rahimi and Recht, 2007] Ali Rahimi and Benjamin Recht. Random features for large-scale kernel machines. In *Adv. Neural Inf. Process. Syst. (NIPS)*, pages 1177–1184, 2007.

[Rajasekaran *et al.*, 2017] Siddharthan Rajasekaran, Jinwei Zhang, and Jie Fu. Inverse reinforce learning with nonparametric behavior clustering. *ArXiv preprint*, abs/1712.05514, 2017.

[Ramachandran and Amir, 2007] Deepak Ramachandran and Eyal Amir. Bayesian inverse reinforcement learning. In *Proc. IJCAI*, pages 2586–2591, 2007.

[Ramponi *et al.*, 2020] Giorgia Ramponi, Amarildo Likmeta, et al. Truly batch model-free inverse reinforcement learning about multiple intentions. In *Proc. AISTATS*, volume 108 of *Proceedings of Machine Learning Research*, pages 2359–2369, 2020.

[Rand, 1971] William M Rand. Objective criteria for the evaluation of clustering methods. *J. of the American Statistical association*, 66(336):846–850, 1971.

[Rousseeuw, 1987] Peter J Rousseeuw. Silhouettes: a graphical aid to the interpretation and validation of cluster analysis. *J. of computational and applied mathematics*, 20:53–65, 1987.

[Sanford *et al.*, 2023] Clayton Sanford, Daniel J Hsu, and Matus Telgarsky. Representational strengths and limitations of transformers. *Advances in Neural Information Processing Systems*, 36:36677–36707, 2023.

[Snoswell *et al.*, 2021] Aaron J Snoswell, Surya PN Singh, and Nan Ye. Limiirl: lightweight multiple-intent inverse reinforcement learning. 2021.

[Tancik *et al.*, 2020] Matthew Tancik, Pratul P. Srinivasan, et al. Fourier features let networks learn high frequency functions in low dimensional domains. In *Adv. Neural Inf. Process. Syst. (NIPS)*, 2020.

[Tibshirani *et al.*, 2001] Robert Tibshirani, Guenther Walther, and Trevor Hastie. Estimating the number of clusters in a data set via the gap statistic. *J. of the royal statistical society: series b (statistical methodology)*, 63(2):411–423, 2001.

[Traag *et al.*, 2018] Vincent A. Traag, Ludo Waltman, and Neele Jan van Eck. From louvain to leiden: guaranteeing well-connected communities. *ArXiv preprint*, abs/1810.08473, 2018.

[Vaswani *et al.*, 2017] Ashish Vaswani, Noam Shazeer, Niki Parmar, Jakob Uszkoreit, Llion Jones, Aidan N. Gomez, Łukasz Kaiser, and Illia Polosukhin. Attention is all you need. In *Adv. Neural Inf. Process. Syst. (NIPS)*, pages 5998–6008, 2017.

[Vivekanandan *et al.*, 2025] Abhishek Vivekanandan, Christian Hubschneider, and J Marius Zöllner. Contrast & compress: Learning lightweight embeddings for short trajectories. 2025.

[Wang and Isola, 2020] Tongzhou Wang and Phillip Isola. Understanding contrastive representation learning through alignment and uniformity on the hypersphere. In *Proc. of ICML*, volume 119 of *Proceedings of Machine Learning Research*, pages 9929–9939, 2020.

[Wang *et al.*, 2024] Ao Wang, Fengyuan Sun, et al. [cls] token tells everything needed for training-free efficient mllms. 2024.

[Wang, 2010] Junhui Wang. Consistent selection of the number of clusters via crossvalidation. *Biometrika*, 97(4):893–904, 2010.

[Xu *et al.*, 2003] Wei Xu, Xin Liu, and Yihong Gong. Document clustering based on non-negative matrix factorization. *Proc. of the 26th annual Int. ACM SIGIR Conf. on Research and development in informaion retrieval*, 2003.

[Xu *et al.*, 2019] Da Xu, Chuanwei Ruan, Evren Körpeoglu, Sushant Kumar, and Kannan Achan. Self-attention with functional time representation learning. In *Adv. Neural Inf. Process. Syst. (NIPS)*, pages 15889–15899, 2019.

[Zheng *et al.*, 2022] Jianqiao Zheng, Sameera Ramasinghe, et al. Trading positional complexity vs deepness in coor-

dinate networks. In *European Conf. on Computer Vision*, pages 144–160. Springer, 2022.

[Ziebart *et al.*, 2008] Brian D. Ziebart, Andrew L. Maas, et al. Maximum entropy inverse reinforcement learning. In *Proc. of AAAI*, pages 1433–1438, 2008.

[Zou *et al.*, 2024] Yixiong Zou, Shuai Yi, Yuhua Li, and Ruixuan Li. A closer look at the CLS token for cross-domain few-shot learning. In *Adv. Neural Inf. Process. Syst. (NIPS)*, 2024.

A Appendix

In this Appendix, we provide further material regarding the CoMI-IRL paper, including details on the environments (Section B), the Behavioral Encoder architecture (Section C), hyperparameters D and the graph-based clustering algorithm (Section E). We provide further results in Section F, including an ablation study on the architecture and loss components introduced in the main paper, and further considerations on the effect of the Jacobian Reweighting. Finally, we report the average wall-clock time of CoMI-IRL and Ess-InfoGAIL for the considered environments.

B Environments

Reacher consists a 2-Degrees of Freedom(DoF) robot arm which goal is to move the robot’s end effector close to a target position. Pusher consists a 4-DoF robot arm which goal is to move a target cylinder to a goal position using the robot’s end effector. Both environments have six goals and the goal location has been removed from the observation [Fu *et al.*, 2023]. Walker-2D is a 6-DoF bipedal robot consisting of two legs and feet attached to a common base which goal is to make coordinate both sets of legs and feet to move the robot in the right direction, including running forward, running backward and balancing.

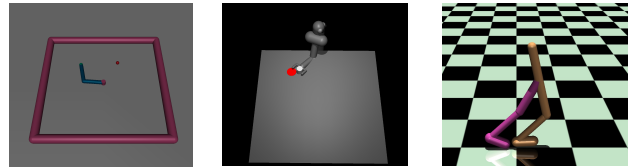


Figure 3: **Left to Right:** Reacher, Pusher, Walker-2D.

C Additional Architecture Details

We presented the architecture of the Behavioral Encoder (BE) in Section 3.1 of the main paper. As trajectories might contain high-frequency elements, and Multi-Layer Perceptrons (*MLPs*) knowingly struggle with high-frequency functions [Rahaman *et al.*, 2019], we use Random Fourier Features with Gaussian mapping (*RFF*) [Rahimi and Recht, 2007; Xu *et al.*, 2019; Zheng *et al.*, 2022; Li *et al.*, 2021]. In each head, this mapping injects a rich set of sinusoidal features at multiple random orientation and frequencies to overcome known *MLP* spectral bias towards low-frequency functions so that, for each $s_{\tau_i}^j \in S_{\tau_i}$ and $a_{\tau_i}^j \in A_{\tau_i}$,

$$RFF(s_{\tau_i}^j) = [\sin(2\pi s_{\tau_i}^j W), \cos(2\pi s_{\tau_i}^j W)]^T, W \sim \mathcal{N}(0, \sigma^2), \quad (6)$$

with σ chosen as a hyperparameter. The output is subsequently processed by a shallow *MLP*, and then followed by a 1D (*CNN*) to capture short-range temporal patterns within the behavioral trajectory, ensuring local coherency. Our approach benefits from this technique both for the internal *MLPs* in the Transformer, and because *RFF* can be seen as a generalized case of the sinusoidal positional encoding [Tancik *et al.*, 2020] needed by the transformer to have information on the order of the sequence.

Hyperparameter	Value
batch_size	256
gen.replay.buffer.capacity	2048
n_disc_updates_per_round	32
reward_hid_sizes	(32,)
potential_hid_sizes	(32, 32)
PPO batch_size	64
PPO ent_coef	0.01
PPO learning_rate	3.0e-4
PPO gamma	0.99
PPO clip_range	0.2
PPO n_epochs (SB3 PPO)	10
total.timesteps (per-cluster)	250000 (1.5M for Walker)

Table 5: AIRL hyperparameters / configuration used in experiments.

D Implementation Details

In this section, we report the hyperparameters used in our experiments for AIRL and GAIL (Table 5), for Ess-InfoGAIL (Table 6), and for the encoder (Table 7). The agents are learned using the imitation library [Gleave *et al.*, 2022] and Stable-Baselines3 [Raffin *et al.*, 2021], while we use the original repository for Ess-InfoGAIL.

Hyperparameter	Value
use_obs_norm	True
auto_lr	True
rollout_length	5000
batch_size	1000
num_steps	2000000
eval_interval	200000
obs_horizon	8
obs_his_steps	1
im_ratio	1
surrogate_loss_coef	4.0
disc_grad_penalty	0.1
value_loss_coef	5.0
disc_coef	20
us_coef	1.0
ss_coef	4.0
info_max_coef1	3.0
info_max_coef2	0.05
info_max_coef3	0.5
begin_weight	20
reward_i_coef	1.0
reward_us_coef	0.1
reward_ss_coef	0.1
reward_t_coef	0.005
epoch_ppo	20
epoch_disc	50
epoch_prior	1
lr_actor	3e-3
lr_critic	3e-3
lr_prior	3e-3
lr_disc	5e-3
lr_q	1e-2

Table 6: Hyperparameters used for Ess-InfoGAIL.

Hyperparameter	Reacher-v4	Pusher-v4	Walker2d-v4
lr	1.0e-4	1.0e-4	5.0e-4
emb_dim	32	32	32
input_channels	6	20	17
max_len	50	100	100
num_heads	4	4	4
nlayers	2	2	2
d_hid	1024	1024	1024
loader_batch	64	32	64
dropout	0.1	0.1	0.1
gaussian_m_state	64	64	64
gaussian_σ_state	0.01	0.001	0.001
gaussian_m_action	32	32	32
gaussian_σ_action	0.1	0.001	0.001
α_training	0.5	0.5	0.5
β_training	1.0	1.0	1.0
γ_training	0.5	0.5	0.5
δ_training	1.0	1.0	1.0
epochs_training	100	100	100
epochs_finetuning	100	100	100

Table 7: Behavioral Encoder hyperparameters used for Reacher / Pusher / Walker.

E Graph-Based Clustering Description

This appendix provides detailed descriptions of the graph-based clustering methods used in CoMI-IRL: the joint k -resolution sweep for the main clustering and the two-stage target-aware clustering for post-finetuning adaptation.

E.1 Joint k -Resolution Sweep

After training the behavior encoder, we cluster trajectory embeddings using graph-based community detection. Our approach operates on the graph structure of the embedding space, making it suitable for continuous behavioral manifolds where modes may not have clear density gaps.

Graph Construction Given N trajectory, we take the L2-normalized embeddings $\{z_i\}_{i=1}^N$ and we construct a weighted k -nearest neighbor graph $\mathcal{G} = (V, E, W)$. For each node i , we find its k nearest neighbors using cosine distance and assign RBF kernel weights based on cosine similarity:

$$w_{ij} = \exp\left(\frac{\text{sim}(z_i, z_j)}{\sigma}\right), \quad \text{sim}(z_i, z_j) = 1 - d_{\text{cos}}(z_i, z_j) \quad (7)$$

where $d_{\text{cos}}(z_i, z_j) = 1 - \tilde{z}_i^\top \tilde{z}_j$ and $\sigma = 1.0$. We make the graph undirected by taking the maximum weight: $w_{ij} = \max(w_{ij}, w_{ji})$.

Automatic Structure Detection Before applying community detection, we check if the graph naturally decomposes into isolated components. For $k \in \{15, 30, 50, 75\}$, we compute the connected components of the k -NN graph. If multiple significant components exist (size $\geq \text{min_cluster_size}$), use them directly as clusters, otherwise proceed to the joint sweep. This handles environments where modes form distinct, well-separated islands in the embedding space (e.g., Reacher-v4, Pusher-v4).

Joint k -Resolution Sweep For clusters spread out on a continuous manifold (e.g., Walker-2D), we jointly optimize over the graph connectivity parameter k and the Leiden resolution parameter γ , following Algorithm 1.

Algorithm 1 Joint k -Resolution Sweep

Require: Embeddings Z , range $[k_{\min}, k_{\max}]$, resolution set Γ , min cluster size m

Ensure: Cluster labels, optimal (k^*, γ^*)

- 1: $\mathcal{R} \leftarrow \emptyset$ {Results collection}
- 2: **for** $k \in \text{linspace}(k_{\min}, k_{\max}, n_k)$ **do**
- 3: Build k -NN graph \mathcal{G}_k
- 4: **for** $\gamma \in \Gamma$ **do**
- 5: $\ell_{k,\gamma} \leftarrow$ Leiden clustering with resolution γ
- 6: Filter clusters with size $< m$ as noise
- 7: $\mathcal{R} \leftarrow \mathcal{R} \cup \{(k, \gamma, \ell_{k,\gamma})\}$
- 8: **end for**
- 9: **end for**
- 10: **Stability-based Selection:**
- 11: **for** each $(k, \gamma) \in \mathcal{R}$ **do**
- 12: $\mathcal{N}_{k,\gamma} \leftarrow$ neighbors with $|k' - k| \leq 15$ or $|\gamma' - \gamma| \leq 0.3$
- 13: $\text{stability}_{k,\gamma} \leftarrow \frac{1}{|\mathcal{N}_{k,\gamma}|} \sum_{(k', \gamma') \in \mathcal{N}_{k,\gamma}} \text{ARI}(\ell_{k,\gamma}, \ell_{k', \gamma'})$
- 14: **end for**
- 15: $(k^*, \gamma^*) \leftarrow \arg \max_{k,\gamma} \text{stability}_{k,\gamma}$
- 16: **return** $\ell_{k^*, \gamma^*}, (k^*, \gamma^*)$

The resolution set used is $\Gamma = \{0.01, 0.025, 0.05, 0.1, 0.15, 0.2, 0.25, 0.3, 0.5, 0.7, 1.0, 1.5, 2.0\}$. Of the tested environments, Pusher and Reacher did not require the joint sweep as their structure already decomposed into isolated components. Further details are provided in Section G.

Leiden Community Detection The Leiden algorithm [Traag *et al.*, 2018] optimizes modularity with a resolution parameter:

$$Q_\gamma = \frac{1}{2m} \sum_{ij} \left[A_{ij} - \gamma \frac{k_i k_j}{2m} \right] \delta(c_i, c_j) \quad (8)$$

where A_{ij} is the adjacency weight, $k_i = \sum_j A_{ij}$ is the weighted degree, $m = \frac{1}{2} \sum_{ij} A_{ij}$ is the total edge weight, c_i is the community of node i , and γ controls granularity (higher values yield more clusters).

Rather than selecting by a single metric, we use partition stability as the primary criterion. For each (k, γ) configuration, we compute the average Adjusted Rand Index (ARI) between its partition and those of neighboring configurations in parameter space. Configurations whose partitions are robust to small parameter perturbations receive higher stability scores. This approach avoids over-fitting to specific parameter choices and identifies genuine cluster structure.

Jacobian-Based Edge Reweighting For environments with continuous behavioral manifolds, embedding similarity alone may not separate subtly distinct modes. In all environments, we augment edge weights with Jacobian-based behavioral features. For each trajectory, we compute:

- State differences: $\Delta s_t = s_{t+1} - s_t$

- Control sensitivity: $\gamma_t = \|\Delta s_t\| / (\|a_t\| + \epsilon)$
- Covariance-based features from $\text{Cov}(\Delta s, a)$

The resulting 8-dimensional feature vector captures:

- Mean/std/max of control sensitivity
- Temporal variance of sensitivity
- Top singular value and ratio from state-action covariance
- Mean/std of action magnitude

Given these statistical features $\{b_i\}$, we update edge weights:

$$w_{ij}^{\text{new}} = w_{ij} \cdot [1 + \alpha \cdot (2 \cdot b_{ij} - 1)] \quad (9)$$

where $w_{ij}^{\text{behav}} = \exp(-\|b_i - b_j\|^2 / 2\sigma_b^2)$ and $\alpha \in [0, 1]$ controls the behavioral contribution, which we set at 0.3. We modulate edge weights by behavioral similarity: edges between trajectories with similar dynamics $b_{ij} > 0.5$ are strengthened, while edges between behaviorally dissimilar trajectories $b_{ij} < 0.5$ are weakened.

Before deciding to use Jacobian features, we test if they are redundant with the learned embeddings by computing the Pearson and Spearman correlation between embedding-based and Jacobian-based pairwise similarities. If the average correlation exceeds 0.7, Jacobian features are skipped as the encoder already captures the relevant dynamics. However, all tests showed an average correlation lower than 0.45, meaning that the Jacobian features are capturing different information.

After clustering, we build a registry storing per-cluster metadata, which is used for novel detection:

$$\text{Registry}[k] = \begin{cases} \mu_k = \frac{1}{|C_k|} \sum_{i \in C_k} \tilde{z}_i & (\text{L2-normalized centroid}) \\ r_k^{95} = \text{quantile}_{95}(\{d_{\text{cos}}(\tilde{z}_i, \mu_k)\}_{i \in C_k}) & (\text{radius}) \\ n_k = |C_k| & (\text{count}) \end{cases} \quad (10)$$

E.2 Two-Stage Clustering Details

After finetuning the encoder on combined seen and online data, the embedding space shifts due to adaptation. This invalidates baseline cluster labels computed in the pre-finetuning space. We address this with a two-stage procedure that leverages knowledge of the expected baseline structure.

Let f_θ denote the baseline encoder and $f_{\theta'}$ the finetuned encoder. For a seen trajectory τ , we can denote the baseline embedding as $z = f_\theta(\tau)$ and the finetuned embedding as $z' = f_{\theta'}(\tau)$.

Despite stability regularization, $z \neq z'$. More critically, the relative positions of clusters may change. A key factor is that we know the expected number of clusters K_{baseline} from before the finetuning. Even though embeddings have drifted, the relative separability of seen modes is typically preserved. We re-cluster *only the seen data* $Z_{\text{seen}} = \{z'_i\}_{i=1}^{N_{\text{seen}}}$ using target-aware selection, following Algorithm 2.

The scoring function $-2 \cdot |n_c - K| + s$ heavily penalizes deviation from the target cluster count while still rewarding cluster quality via silhouette. Using the recovered cluster structure from the first stage, we assign online trajectories following Algorithm 3.

Algorithm 2 Stage 1: Target-Aware Recovery

Require: Finetuned seen embeddings Z_{seen} , target K_{baseline}
Ensure: Recovered labels, centroids, radii

- 1:
- 2: // Check for isolated components first
- 3: **for** $k \in \{15, 30, 50, 75\}$ **do**
- 4: Build k -NN graph, compute connected components
- 5: Count significant components (size $\geq m$)
- 6: **if** $n_{\text{significant}} = K_{\text{baseline}}$ **then**
- 7: Use components as recovered clusters
- 8: **return**
- 9: **end if**
- 10: **end for**
- 11:
- 12: // Target-aware (k, γ) sweep
- 13: $\mathcal{R} \leftarrow \emptyset, \mathcal{E} \leftarrow \emptyset$ {All results, exact matches}
- 14: **for** $(k, \gamma) \in \text{SearchGrid}$ **do**
- 15: Run Leiden, filter small clusters
- 16: $n_c \leftarrow$ number of valid clusters
- 17: Compute silhouette s
- 18: $\mathcal{R} \leftarrow \mathcal{R} \cup \{(k, \gamma, n_c, s, \text{labels})\}$
- 19: **if** $n_c = K_{\text{baseline}}$ **then**
- 20: $\mathcal{E} \leftarrow \mathcal{E} \cup \{|\mathcal{R}| - 1\}$
- 21: **end if**
- 22: **end for**
- 23:
- 24: // Selection
- 25: **if** $\mathcal{E} \neq \emptyset$ **then**
- 26: Select from \mathcal{E} with best silhouette
- 27: **else**
- 28: Score $= -2 \cdot |n_c - K_{\text{baseline}}| + s$
- 29: Select configuration with best score
- 30: **end if**
- 31:
- 32: Compute recovered centroids $\{\mu_k^{\text{rec}}$ and radii $\{r_k^{\text{rec}}$
- 33: **return** labels, centroids, radii

The threshold θ controls sensitivity to novel modes. We set $\theta = 0.1$ on Reacher and Pusher, as clusters are well-separated, while we set $\theta = 0.05$ on Walker, as the continuous manifold creates the risk of over-assignment to existing clusters at mode boundaries. The recovered radius r_k^{rec} is computed as the 95th percentile of within-cluster cosine distances, expanded by factor 1.2 to account for minor embedding shifts.

Output Structure The two-stage procedure produces:

- **Recovered clusters** (IDs $0, \dots, K_{\text{baseline}} - 1$): Correspond to baseline modes in the new space. Previously trained IRL agents are directly assigned.
- **Novel clusters** (IDs $\geq K_{\text{baseline}}$): Contain trajectories from genuinely new behavioral modes. New IRL agents are trained for these.

Algorithm 3 Stage 2: Anchored Assignment

Require: Online embeddings Z_{online} , recovered centroids $\{\mu_k^{\text{rec}}$, radii $\{r_k^{\text{rec}}$, threshold θ
Ensure: Labels for online data, novel cluster IDs

- 1:
- 2: **for** each online embedding z **do**
- 3: $d_k \leftarrow 1 - \frac{z^T \mu_k^{\text{rec}}}{\|z\| \|\mu_k^{\text{rec}}\|}$ for all k
- 4: **if** $\min_k d_k \leq \theta \cdot r_k^{\text{rec}}$ **then**
- 5: Assign to nearest cluster: $\ell \leftarrow \arg \min_k d_k$
- 6: **else**
- 7: Mark as novel candidate
- 8: **end if**
- 9: **end for**
- 10:
- 11: // Sub-cluster novel candidates
- 12: **if** $n_{\text{novel_candidates}} \geq m$ **then**
- 13: Build k -NN graph on novel candidates
- 14: Compute connected components
- 15: **if** multiple components **then**
- 16: Each component \rightarrow separate novel cluster
- 17: **else**
- 18: Run Algorithm 1 with restricted grid search
- 19: **end if**
- 20: **end if**
- 21: **return** labels, novel_cluster_ids

E.3 Hyperparameters

	Description	Value
k_{min}	Min neighbors for graph	$\max(5, N/50)$
k_{max}	Max neighbors for graph	$\min(100, N/3)$
σ	RBF kernel bandwidth	1.0
m	Min cluster size	$\max(5, 0.02 \cdot N)$
α_{behav}	Jacobian weight	0.3
θ_{novelty}	Novelty threshold	0.05–0.1
$r_k^{95 \text{ exp}}$	Factor for recovered radii	1.2

Table 8: Graph clustering hyperparameters

F Additional Results

F.1 Ablations

To validate the architectural choices of the pre-processing block composed by *RFF+MLP+CNN* (called *preBlock* in the results) within the BE, we run an ablation study over 3 seeds. To validate the loss composition of global contrastive, segment contrastive and DIM [Hjelm *et al.*, 2019] regularization, we run an ablations over 10 seeds, reporting in Table 9 the clustering quality of each version. While the versions with and without the DIM regularization are very similar (BE+CS and BE+DCS), we use the full version (BE+DCS) in our experiments as it showed higher stability and slightly better performance in most cases.

Table 9: **Ablation Study.** Impact of architecture (removing the $RFF+MLP+CNN$ preprocessing) over 3 seeds and loss components on clustering quality over 10 seeds. Loss keys: **C**=Global Contrastive, **D**=DIM, **S**=Segment/Pairwise.

Configuration	NMI	ARI	Sil
Reacher-v4			
<i>Architecture</i>			
BE (Full)	0.84 \pm 0.00	0.63 \pm 0.00	0.87 \pm 0.06
BE \ (preBlock)	0.36 \pm 0.32	0.21 \pm 0.23	0.29 \pm 0.25
<i>Loss Design</i>			
BE + C	0.44 \pm 0.10	0.26 \pm 0.08	0.39 \pm 0.07
BE + DC	0.46 \pm 0.14	0.27 \pm 0.10	0.37 \pm 0.09
BE + CS	0.82 \pm 0.04	0.60 \pm 0.06	0.82 \pm 0.10
BE + DCS	0.83\pm0.01	0.62\pm0.02	0.84\pm0.06
Pusher-v4			
<i>Architecture</i>			
BE (Full)	1.0 \pm 0.00	1.0 \pm 0.00	0.99 \pm 0.01
BE \ (preBlock)	1.0 \pm 0.00	1.0 \pm 0.00	0.94 \pm 0.01
<i>Loss Design</i>			
BE + C	0.85 \pm 0.10	0.77 \pm 0.18	0.47 \pm 0.10
BE + DC	0.81 \pm 0.22	0.73 \pm 0.32	0.50 \pm 0.16
BE + CS	0.99 \pm 0.01	0.99 \pm 0.01	0.97 \pm 0.02
BE + DCS	1.0\pm0.00	1.0\pm0.00	0.98\pm0.01
Walker2d-v4			
<i>Architecture</i>			
BE (Full)	0.75 \pm 0.05	0.77 \pm 0.07	0.60 \pm 0.01
BE \ (preBlock)	0.73 \pm 0.05	0.69 \pm 0.10	0.37 \pm 0.02
<i>Loss Design</i>			
BE + C	0.42 \pm 0.04	0.32 \pm 0.04	0.49 \pm 0.04
BE + DC	0.42 \pm 0.03	0.34 \pm 0.06	0.49 \pm 0.05
BE + CS	0.80\pm0.06	0.82\pm0.06	0.57 \pm 0.04
BE + DCS	0.79 \pm 0.06	0.80 \pm 0.10	0.57\pm0.03

F.2 Jacobian Reweighting Effect

For each environment, we present the effects of applying the Jacobian reweighting of graph edges in terms of edge weight. While for Pusher and Reacher (Figure 4 and Figure 5) the impact is less prominent due to the already well-conditioned structure of the two spaces, so that the number of increased edges is very small (1% for Pusher and 5% for Reacher), in Walker (Figure 6) the reweighting has a higher effect, since it has more heterogeneous action effects on the different features. Between clusters, most edges are decrease, noticeable by the lighter color shade, while the 13% of increased edges are mostly within-cluster edges.

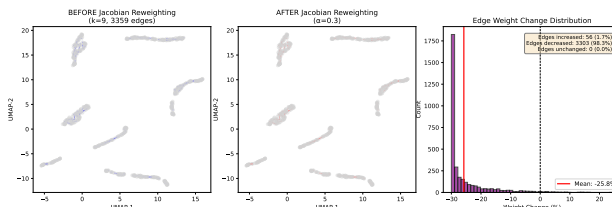


Figure 4: Jacobian Edge Reweighting on Pusher.

G Computational considerations

We ran our experiments on a 2020 MacBook Pro with 2 GHz Quad-Core Intel Core i5. In the following Table, we report the average wall-clock times of Ess-InfoGAIL and CoMI-IRL

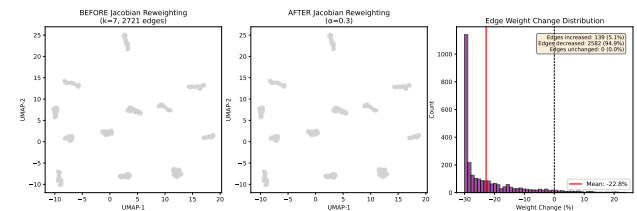


Figure 5: Jacobian Edge Reweighting on Reacher.

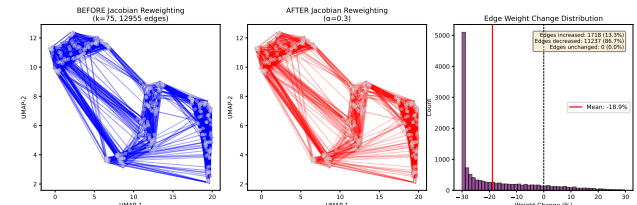


Figure 6: Jacobian Edge Reweighting on Walker.

(divided by phase) for each environment in Table 6. It is important to notice that while the BE’s training on GPU would take much less (\sim 5 minutes), transformers training time also increases with the amount of training samples in the dataset.

	Reacher	Pusher	Walker
CoMI-IRL			
BE	\sim 16	\sim 25	\sim 17
Clustering (s)	\sim 0	\sim 0	\sim 20
IRL	\sim 14	\sim 14	\sim 48
Total	\sim 30	\sim 39	\sim 65
Ess-InfoGAIL			
$K = 3$	\sim 35	\sim 39	\sim 55
$K = 6$	\sim 41	\sim 46	\sim 76
$K = 12$	\sim 48	\sim 58	\sim 103

Table 10: Wall-clock time for the different components of CoMI-IRL and total, and the Ess-InfoGAIL experiments with different values of K . While all values are reported in minutes, the clustering values are reported in seconds. In CoMI-IRL’s IRL phase, the reported time is the time of a single cluster, as it’s fully parallelizable.